Silhouette-based 3D Model for Zebrafish High-throughput Imaging

Yuanhao Guo[1], Wouter J. Veneman[2], Herman P. Spaink[2] and Fons J. Verbeek[1]
[1] Imaging and BioInformatics Section, LIACS, Leiden University, The Netherlands
e-mail: {y.guo.3, f.j.verbeek}@liacs.leidenuniv.nl
[2] Department of Animal Sciences and Health, Institute of Biology, Leiden University, The Netherlands
e-mail: {w.j.veneman, h.p.spaink}@biology.leidenuniv.nl

***Abstract*— Good estimations of volume and surface area are important to biological systems measurement. In this paper we develop a 3D reconstruction from evenly sampled axial views in order to enable the volume and surface area measurement. We develop this system for high throughput applications with the zebrafish model system. The VAST BioImager is specifically developed for this purpose and with this system the axial views can be produced. Silhouettes derived from the axial sequence are shape priors which can be directly used to solve the camera calibration problem that is required for the accurate 3D reconstruction. Nonlinear optimisation algorithms have shown to be suitable for the further development of the reconstruction problem. The method proposed in this paper can be included in a measurement pipeline that is used in all kinds of high throughput applications in the zebrafish field. From the 3D reconstruction features can be derived that will contribute to the phenotyping of zebrafish.**

***Keywords*— VAST BioImager, Zebrafish, 3D model, Shape carving, Volume and surface area measurement.**

I. Introduction

In modern molecular genetics the zebrafish is a popular model system. In early development zebrafish are transparent and therefore easily studied through different microscopies. Another advantage is that it is easy to obtain large offspring, e.g. $>$ 200 embryos per lay. Among other characteristics, this has made the zebrafish suitable for high throughput studies in the area of toxicology, infectious diseases and drug targeting. In this manner, on a systematic basis large amounts of different targets can be evaluated. The zebrafish, and in particular the zebrafish embryo and larva are studied with different microscopies, such as traditional bright field microscope, but more frequently, fluorescent microscope, as there is an large amount of fluorescent markers and genetically engineered zebrafish available for research purposes. With fluorescent tags specific signals can be detected and thus measured. For high throughput [1], in general 2D imaging techniques are employed [2], but descriptive measurements sometimes require 3D imaging techniques. With the confocal laser scanning microscope (CLSM) 3D images of the zebrafish can be obtained; however, CLSM is not directly suitable for high throughput systems. In order to accomplish high throughput systems for zebrafish, the Vertebrate Automated Screening Technology (VAST BioImager) has been developed [3]. A VAST BioImager unit is used for the automated dispatching of zebrafish embryos/larva to an imaging system, i.e. a fluorescence microscope or a CLSM. To that end, one-by-one the zebrafish are loaded into a tiny capillary and through a pumping system the specimen is put into the field of view of the imager. The capillary is mounted in a holder that can be rotated with stepper motors so that the specimen can be viewed from any viewpoint. In this manner a full revolution of the object under study, i.e. the zebrafish, can be obtained. In Fig. 1 (a) examples of such views are depicted.

In order to obtain information on the volume and the surface area of the object, we have developed the possibility to produce a 3D reconstruction from a set of views of the object in addition to any other imaging that might be applied. The development required studying and assessing a number of techniques for 3D reconstruction from multiple views of an identical object. The concept of shape carving [4], a.k.a. visual hull construction [5], is quite well developed in the area of computer vision – typically to reconstruct a 3D object from a range of views of the object that are in fact evenly spaced sampled around the object. For our purpose, we will produce a 3D model from the silhouette of the object as it is observed in the capillary in each of the orientations. The VAST BioImager can generate different samplings for a set of axial views and this will be employed in order to obtain our multiple-view image sequences. The silhouettes are generated from a segmentation of each individual view and the binary masks are used in the visual hull construction. In this paper we will further elaborate how we have realized this. Each image sequence will generate a 3D model and we intend to build an understanding of what will be an efficient and accurate sampling density for the image sequence to produce an accurate 3D model.

II. Related Work

From the perspective of computer vision, silhouette-based 3D reconstruction is a well studied topic for the last decades. Simple parallel projections intersection [6] is proposed to confine a bounding volume which is the final 3D reconstruction. An octree structure is then proposed to refine the 3D volumetric representation [7]. Parent 3D representative cubics whose projected correspondences are on the border of the silhouettes will be split into smaller scales until convergence. This method accelerates the computation and increases the representation accuracy. With the introduction of Visual Hull (VH) concept

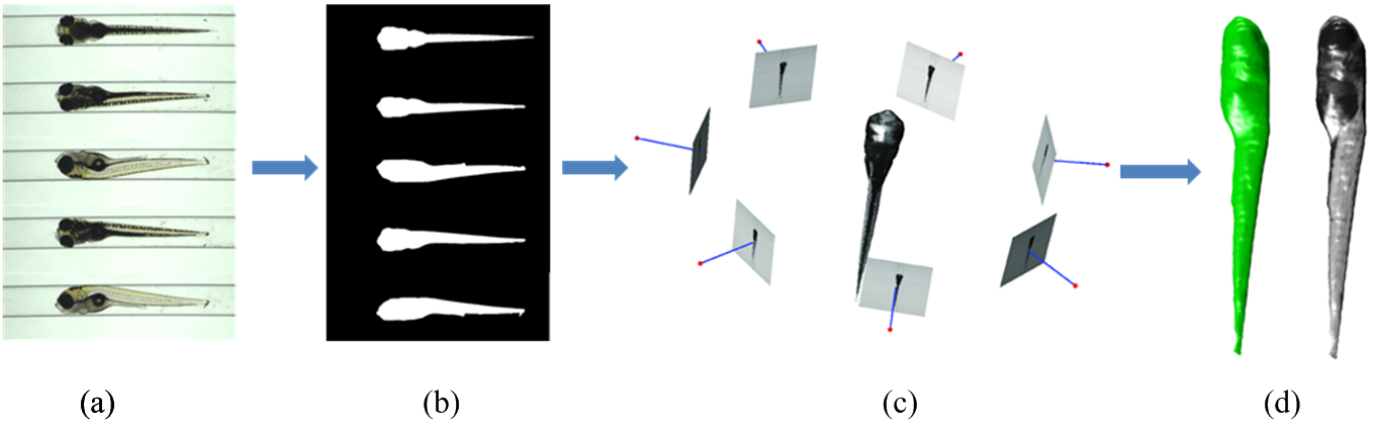

Fig. 1. 3D zebrafish model framework. (a) The original zebrafish images in different poses. (b) The corresponding silhouette. (c) The VAST BioImager imaging scheme in a revolution. Bold red point: camera center. Bold blue line: camera principle. 2D image: camera image plane. The 3D reconstruction is generated from the cone-shaped projections intersection by back-projecting each of the silhouettes to the 3D world. (d) The reconstructed 3D zebrafish model.

[5], the silhouette-based 3D reconstruction research has attracted lots of attention [8], [9], [10], [11], [12]. Kutulakos and Seitz [4] define a unified framework to construct a 3D model from multi-view silhouettes. Camera projection properties are included to genuinely model a scene. Better quality 3D reconstruction is obtained by fusing silhouettes and vision information [13]. Based on the framework of active contours, several push-pull forces are derived from the object visual hull and image texture. The best 3D reconstruction corresponds to the minimum of a fused cost function. A different approach is taken by introducing a Bayesian probability model [14]. This approach computes the probability of occurance of a 3D shape given a set of images and a set of possible 3D surfaces. The variational-based level set method is employed to solve this probabilistic maximisation problem. From this starting point, a more general solution [15] has been developed. A convex penalizer leads the cost function to be continuously convex, which can be globally optimized using standard gradient descent techniques. What should be noted is that camera calibration is required for those methods, because the predicted 3D object must be accurately projected to the image set. This can be easily realized in current imaging system according to [16], [17]. With different view images from some particular patterns, such as checkerboard with interval black and white bins, camera properties including focal length and scaling factor, etc. can be computed by solving a linear function, which is , however, infeasible in the microscope imaging scheme. Instead, automated camera calibration can be done by optimising a cost function in terms of silhouette coherence which defined as the overlap between projected and original contours [18].

Compared to previous research, our work differs in several aspects. First, this is an initial attempt to apply silhouette-based 3D reconstruction technique in a microscope environment. Second, to our current knowledge, building a well-calibrated multi-view imaging system is difficult and expensive. For our work, the existing VAST BioImager provides an elegant machinery to take images in different views, so that the necessary priors including initial camera configuration can be obtained. Third, we use a different measurement [19] to evaluate the camera configuration. Moreover, the resulting model can be used for animation purposes, such as the modelling of the innate immune system in zebrafish [20]. Importantly, the 3D volume and surface area can be acquired, which offers measurement reference to evaluate the zebrafish development during fluorescent marking and genetically engineering.

The remainder of this paper is organized as follows: Section III interprets how the silhouette-based 3D surface reconstruction algorithm is derived and applied in our work in details. In Section IV illustrates how many views we need to construct a full 3D zebrafish embryo surface and some of the refined reconstructed examples. In Section V, conclusions are mentioned and several possible future developments are briefly discussed.

III. 3D Zebrafish Model Reconstruction

The proposed model is depicted in Fig. 1. The axial views zebrafish embryo images are generated and then segmented to a binary silhouette sequence. A set of voxels, which are initialized to be able to cover the original object, are then projected to each of the masks to calibrate the VAST BioImager camera. With the optimal camera parameters, an optimal 3D model including volume and surface can be reconstructed.

A. Pinhole camera model

Figure 1 (c) demonstrates the VAST BioImager imaging scheme. As other imaging systems, VAST BioImager imaging unit is equipped with a CCD camera. The standard pinhole camera model can be used to illustrate the imaging principle. The mapping between a 3D world point and its corresponding projective 2D image point $\mathbf{X} \in \mathbb{R}^3 \longmapsto \mathbf{x} \in \mathbb{R}^2$ can be modelled as $\mathbf{x} = \mathbf{PX}$. Basically, the projection matrix $\mathbf{P}$ can be decomposed into several components: $\mathbf{P} = \mathbf{K} \cdot \mathbf{R} \cdot [\mathbf{I} \,|\, -\tilde{\mathbf{C}}]$. Specifically,

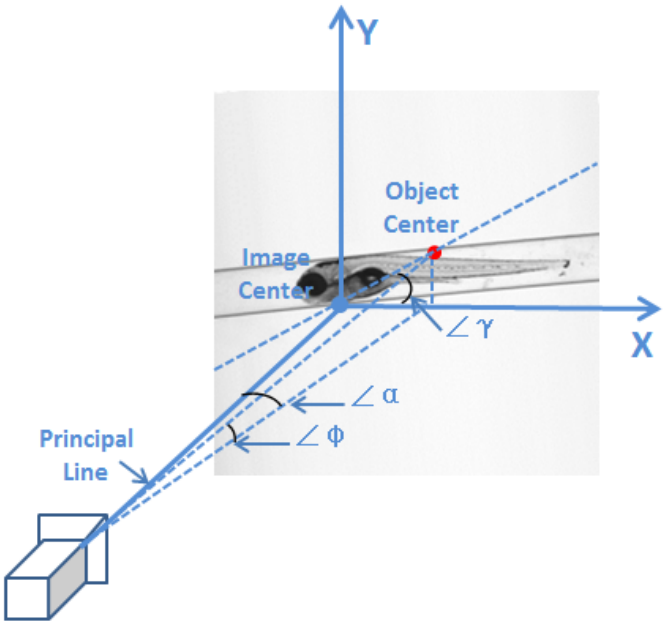

Fig. 2. Camera projection parameterization. Bold red dot: object center. Bold blue dot: image center. Thick blue line in Z-direction: camera principal line. α, γ, ϕ: camera 3D rotations. Each of the camera imaging schemes shown in Fig. 1 (c) can be modelled like this.

$$\mathbf{K} = \begin{bmatrix} f * k_x & 0 & u_x \\ 0 & f * k_y & u_y \\ 0 & 0 & 1 \end{bmatrix} \tag{1}$$

is defined as the intrinsic camera matrix, where f is the focal length, k_x and k_y are scaling factors in x and y direction, and (u_x,u_y) is the image center. For the reason of simplification, we do not consider the camera distortion factors. $\mathbf{R}$ represents the three dimensional rotation matrix which has three degree of freedom separately corresponding to the rotation angles along the three axis which are parameterized in Fig. 2 as $\mathbf{r} = [\alpha, \phi, \gamma]^{\mathrm{T}}$. Taking the rotation around X-axis as an example, the rotation model can be formulated by

$$\mathbf{R_x} = \begin{bmatrix} 1 & 0 & 0 \\ 0 & cos(\phi) & sin(\phi) \\ 0 & -sin(\phi) & cos(\phi) \end{bmatrix}. \tag{2}$$

With the other two directional rotations, the 3D rotation model can be cascaded to $\mathbf{R} = \mathbf{R_x}\mathbf{R_y}\mathbf{R_z}$. As shown in Fig. 1 (c), the camera motion makes a full circulation and the manipulation motor is set up with a fixed step angle. For the i^{th} camera view, it is easy to make a good estimation of its translation as $\tilde{\mathbf{C}}_i = [0, f \cdot cos(\omega_i), f \cdot sin(\omega_i)]^{\mathrm{T}}$, where, the ω_i is defined as $\omega_i = 2(i-1)\pi/n$, where n is the number of axial views. All the parameters are concatenated in a vector $\psi = [f, k_x, k_y, u_x, u_y, \alpha, \phi, \gamma, \omega_1, ..., \omega_{n-1}]$ which is the actual camera configuration.

B. Silhouette-based 3D reconstruction

In principal, a silhouette-based 3D reconstruction only uses masks obtained from the axial images to predict a reasonable object shape. Given an object and a set of camera configurations, multi-view images can be obtained through the standard camera pinhole model which generates a set of cone-shaped projections. Assume the original object is unknown, while the camera configurations and the multi-view silhouettes are known, the original shape can be reconstructed by back-projecting all the masks to 3D world coordinate system. The original object is actually the intersection of all projection cones.

Mathematically, we use the concept of Visual Hull Theory ($\mathcal{VH}$) [4] to illustrate this reconstruction problem. Let $\mathcal{V}$ be an object shape and $Iso(\mathcal{V})$ be the object surface. $v \in \mathcal{V}$ is a voxel within the shape $\mathcal{V}$. Let $\mathcal{S}^j$ be the j^{th} viewpoint silhouette and $\mathbf{P}^j$ $(j = 1, ..., n)$ be the corresponding camera projection matrix. Following the camera projection model, each voxel in $\mathcal{V}$ should be projected onto the j^{th} camera image plane as $x^j = \mathbf{P}^j v$. The voxel v producing the pixel collection of $x^j \cap \mathbf{S}^j \neq \varnothing$ consists the j^{th} estimated 3D shape $\mathcal{V}^{j*}$ which can be formalised as

$$\mathcal{V}^{j*} = \{v \mid (x^j = \mathbf{P}^j v, v \in \mathcal{V}) \cap \mathcal{S}^j \neq \varnothing\}. \tag{3}$$

Given the n projected silhouettes, the optimal object is acquired from the intersection of all back-projections as

$$\mathcal{V}^* = \bigcap_{j=1,...,n} \mathcal{V}^{j*}. \tag{4}$$

For a more efficient implementation, the final shape should be generated through iteration. Given an initial $\mathcal{V}$, the n silhouettes and camera models are considered one by one until the shape converges. So, it is reasonable to reformulate Eqs. 3 and 4 to:

for $t = 1$,

$$\mathcal{V}^{1*} = \mathcal{V} - \{v \mid (x^1 = \mathbf{P}^1 v, v \in \mathcal{V}) \cap \mathcal{S}^1 = \varnothing\}; \tag{5}$$

and for $t = 2$ to n,

$$\mathcal{V}^{t*} = \mathcal{V}^{(t-1)*} - \{v \mid (x^t = \mathbf{P}^t v, v \in \mathcal{V}^{(t-1)*}) \cap \mathcal{S}^t = \varnothing\}. \tag{6}$$

In order to avoid misuse of the parameters, we reparameterize the subscript as t indicating the t^{th} iteration. After total of n iterations, the optimal shape $\mathcal{V}^{n*}$ can be obtained and thereby the associated object surface $Iso(\mathcal{V}^{n*})$.

C. Camera configuration optimization

According to the state-of-art, a multi-view 3D reconstruction is very sensitive to camera calibration. The 3D model reconstruction for zebrafish is even more depending on camera calibration. This is partially due to the large difference between camera focal length and object size. The effects of camera model estimation are depicted in Fig. 3. In many computer

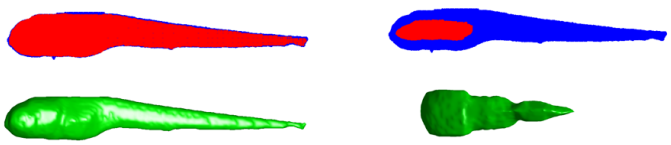

Fig. 3. Camera configuration effects for silhouette-based 3D model reconstruction. Blue area: ground-truth silhouette. Red area: overlap between the projected and the ground-truth mask. Green surface: reconstructed shape. Left column: optimal camera configuration gives maximal overlap area and obtains natural shape. Right column: inaccurate camera configuration gives small overlap area and obtains poor shape.

vision systems, standard image-based methods [16], [17] are involved to solve this problem, while those methods are infeasible in the microscope setup, such as the VAST BioImager, due to the imaging scale. Automated camera calibration without the use of any particular pattern is, however, still possible [18]. The idea is to optimize an energy function by searching the camera configuration space formulated in Section III-A. One can try to maximize the overlap between the projected contours and the ground-truth silhouettes, which is defined as the energy function.

Instead of the silhouette coherence [18], we use another criterion to evaluate the energy function. This is replaced to area coherence [19], expressed as:

$$f(\psi) = \frac{1}{n} \sum_{j=1:n} C(\mathcal{S}^j, x^j), \tag{7}$$

where $C(\mathcal{S}^j, x^j) = \mathcal{S}^j \cap (x^j = \mathbf{P}^j(\psi)v)$. When the optimal estimated 3D reconstruction is projected to the silhouette sequence, the average of all overlap areas should be the maximum. This is also shown in Fig. 3. As a result, the camera parameters optimization problem can be formulated as a maximization problem:

$$\psi^* = \max_{\psi \in \Psi} f(\psi). \tag{8}$$

This optimisation problem is hard to solve by an explicit gradient descent method. However, the entry ψ of the function can be initialised to be a reasonable estimation. For example, the term working distance of the system indicates the focal length, and the image center can be assumed to be the pixel-wise center. The rotation angles will be initialized as zeros. With this initial configuration, evolution algorithms and other derivative-free methods such as the Nelder-Mead simplex method [21] can be employed to maximize Eq. 8. It is not hard to imagine that the computation will be expensive for such a large vector of variables. However, we just need to compute all possible parameters once and the optimal results can be used for the rest of the data except for the camera motion ω. Anyway, even for ω, we already have a first estimation from the first experiment, in such a manner may largely accelerate the subsequent performance.

Table 1. Voxel residual (V_R) volume statistics ($\times 10^{-3} mm^3$).

VSD	Mean	STD	SEM
2	951.79	±140.92	±49.82
4	383.18	±35.91	±12.70
6	338.75	±26.02	±9.20
8	316.38	±20.60	±7.28
10	309.61	±21.24	±7.51
14	305.43	±21.34	±7.54
20	298.98	±21.04	±7.44
28	296.58	±20.37	±7.20
42	293.11	±20.29	±7.17
84	289.21	±19.74	±6.98

STD: standard deviation.
SEM: standard error of the mean.

Table 2. Surface area (A_S) statistics ($\times 10^{-2} mm^2$).

VSD	Mean	STD	SEM
2	1041.24	±52.98	±18.73
4	473.99	±27.74	±9.81
6	427.69	±19.91	±7.04
8	406.23	±17.94	±6.34
10	402.21	±17.94	±6.34
14	398.29	±19.00	±6.72
20	391.91	±17.05	±6.03
28	389.61	±16.40	±5.80
42	386.44	±16.39	±5.79
84	382.53	±15.69	±5.55

IV. Experiments

Based on the pipeline structured in Fig. 1, the system can be implemented by cascading each individual procedure. The axial view images are obtained from VAST BioImager. The silhouettes are generated from a segmentation of each axial views. To this end, the level-set based method [22] is employed due to its flexibility and robustness in various applications. With the masks, the proposed model is performed to calibrate the camera and then generate the 3D model. To facilitate the experiments, we have built a database for zebrafish embryo development. This database contains different staged zebrafish embryos which are imaged by VAST BioImager within 84 almost evenly sampled views. The step angle between each pair of neighbouring views is around 4.3 degree, not exact due to mechanical drift. This problem can be solved as is proposed in Section III-C. In this paper, we use eight six-day-old live zebrafish embryos selected from the database as examples.

A. How many views are needed?

A full revolution motion of the camera is needed to construct an accurate and integral 3D model. It should be noted that the camera is stable for the VAST VAST BioImager. Instead, the object rotates based on a fixed axis. For better interpretation, we allocate the camera around the object in this paper. It is obvious that the larger the view sampling density (VSD) is, i.e. the number of views, from the axial views, the more accurate reconstruction can get. The sampling density of the axial views ensures the point occurances on the object surface to multi-viewed observers. Reconstruction errors caused by silhouettes associated with segmentation noise can be corrected by others

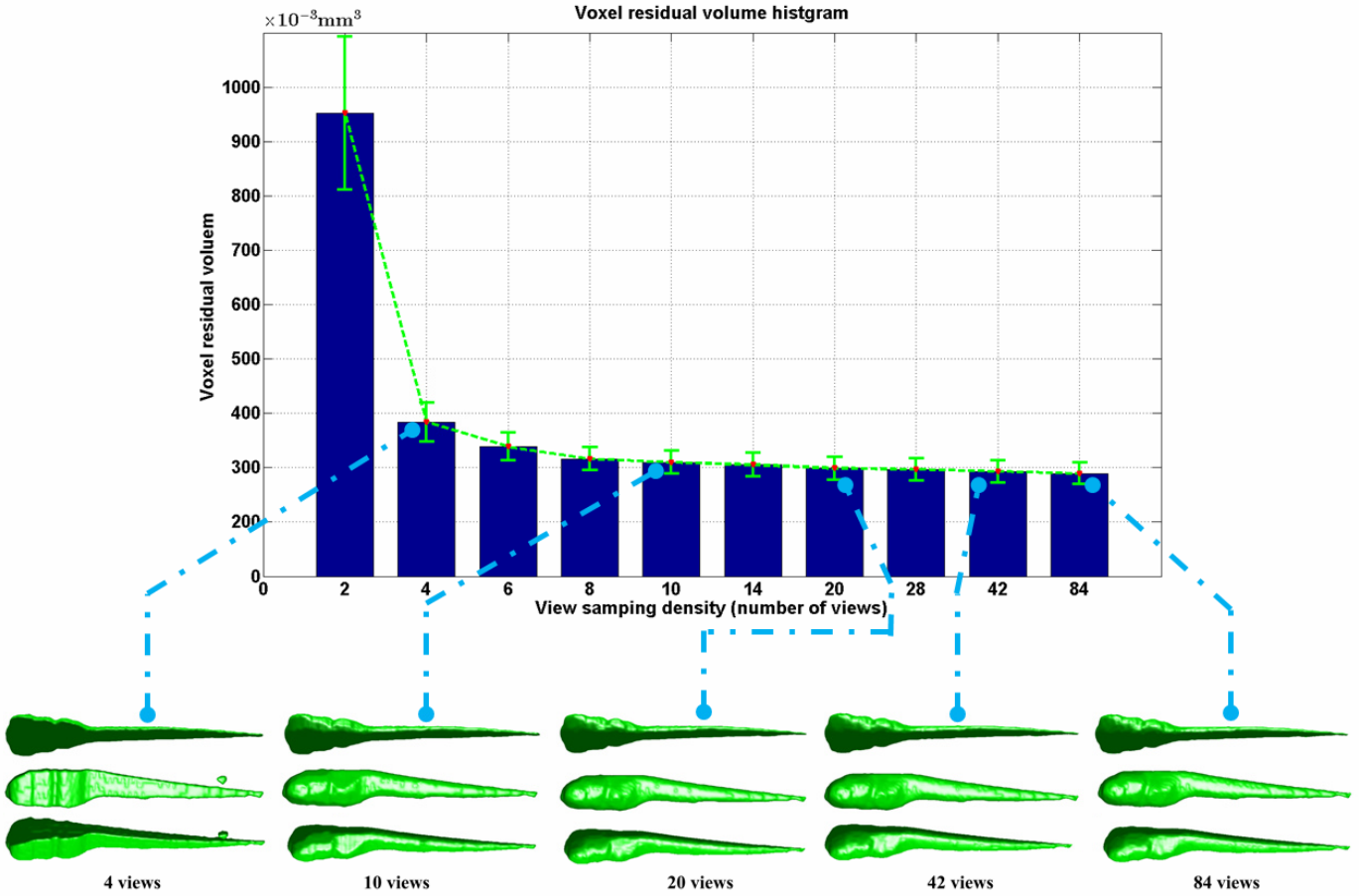

Fig. 4. Figure of merit for the proposed model. Upper row: the voxel residual volume histgram. X direction: views sampling density (VSD). Y direction: remaining voxel volume. The views are sampled almost uniformly from a full circulation. Lower row: some selected 3D zebrafish embryo reconstructions with different VSD. The light blue dash lines indicate the correspondences between the VSD and the reconstructed results

in which the noise may not be present. This experiment will reveal what is an efficient VSD to reconstruct a 3D model. The performance of the proposed method is shown in Fig. 4. In order to obtain a distinct resolution, the initial shape candidate is set as $10E6$ voxels. We gradually increase the VSD beginning with 4. It is obvious that the voxel residual (V_R) volume will reduce along with the increasing VSD. The V_R volume is collected and plotted in the upper row of Fig. 4. The bottom row of Fig. 4 shows some selected reconstructed effects posed in three different perspectives with different VSD.

From Fig. 4, one can see that with increasing VSD, the V_R volume decreases and asymptotically stabilises. In Tables 1 and 2, the same trend can also be seen, i.e. the yield beyond the VSD of 84 is not leading to a particularly better result. In addition, Table 1 and 2 also show the volume and surface area measurement references for future work. From the lower row of Fig. 4, at a VSD of 4, the carved shape is close to the initial voxels shape , i.e. cube, and the edges are very sharp, which is reasonable due to the intersection effect of camera pinhole projections. When the VSD is larger than 10, the reconstructed shape appears natural and the associated surface is smooth. For a VSD of 10, one still can experience either flat or steep homogeneous carving scars in some local regions on the object surface. At a VSD larger than 20, the reconstruction results are good and not much different. Interestingly, a VSD such as 84 causes ”surface wrinkles”. Sophisticated multi-view projections with about every 4.3 degrees recovers a model which tries to satisfy each of the shape priors so as to introduce more noise. According to this experiment, accurate 3D reconstruction results are generated with large VSD. However, with the VSD larger than 20, volume and surface area variation becomes very small and the reconstructed shape and surface visualisation is stable. Considering computation complexity, the conclusion can be made that a VSD of 20 is sufficient to obtain accurate results for our 3D zebrafish embryo model reconstruction problem.

B. Reconstructed 3D zebrafish models

In this experiment we have repeated the proposed method on different zebrafish embryo examples and visualised the reconstructed 3D models. A Zebrafish embryo has a transparent torso. What we can observe is actually its frontal part such as head, some internal structures and black pigmented cells

Fig. 5. Reconstructed and rendered 3D zebrafish models. The first column comes from the profiles and the second column shows the dorsals. The first two rows, the middle two rows and the last two rows present three different individuals respectively.

which are distributed on its backside. As we work with live zebrafish, the physiology is still active and heart beating as well as blood circulation are visible in the microscope. This is one of the reasons of the popularity of the zebrafish model system for studies such as infection and inflammation.

From column 1 in Fig. 5, the zebrafish 3D shape is fully reconstructed and the rendered results apparently show the eyes, ears and spiral cords. We can also see the shape variations from different individuals, which may help to construct more general probabilistic shape models. However, reconstruction imperfection can happen. This has two main causes: the silhouette-based 3D reconstruction depends on image segmentation, and the zebrafish caudal visibility from lateral perspective is difficult. Therefore, the segmentation results are imperfect, and has a deteriorating effect on the reconstructed shape. The other cause is the employment of camera configuration optimisation, which aims to optimise the criterion of coherence area. This criterion somehow does not completely consider the 3D shape fidelity and surface smoothness.

V. Conclusions and Future Work

In this paper we have shown a method for the development of a 3D model of an object from a sequence of axial views. The 3D model is constructed from silhouettes that are segmented from the axial views and subsequently shape carving is used. The VAST BioImager is efficient for providing the axial view sequence of the zebrafish embryo to which our variation of shape carving can be applied. The optimization of an energy function is defined by area coherence and automated camera calibration accomplishes an accurate 3D model. Future developments will be directed to further improve the model construction focusing on removal of imperfections in the segmentation of the axial views. Moreover, the camera calibration procedures can be improved. These improvements will result in an even more efficient and accurate 3D reconstruction.

Acknowledgment

This research is partially funded by Chinese Scholarship Council (CSC) and The Netherlands Organisation for Scientific Research (NWO).

References

[1] WJ Veneman, R Marín-Juez, J de Sonneville, A Ordas, S Jong-Raadsen, AH Meijer, and HP Spaink, "Establishment and optimization of a high throughput setup to study staphylococcus epidermidis and mycobacterium marinum infection as a model for drug discovery," *Journal of visualized experiments: JoVE*, , no. 88, 2014.

[2] AE Nezhinsky and FJ Verbeek, "Pattern recognition for high throughput zebrafish imaging using genetic algorithm optimization," in *5th IAPR Conf. on Pattern Recognition in BioInformatics (PRIB 2010)*, pp. 301–312. Springer, 2010.

[3] C Pardo-Martin, T Chang, BK Koo, CL Gilleland, SC Wasserman, and MF Yanik, "High-throughput in vivo vertebrate screening," *Nature methods*, vol. 7, no. 8, pp. 634–636, 2010.

[4] KN Kutulakos and SM Seitz, "A theory of shape by space carving," *IJCV*, vol. 38, no. 3, pp. 199–218, 2000.

[5] A Laurentini, "The visual hull concept for silhouette-based image understanding," *TPAMI*, vol. 16, no. 2, pp. 150–162, 1994.

[6] WN Martin and J K Aggarwal, "Volumetric descriptions of objects from multiple views.," *TPAMI*, vol. 5, no. 2, pp. 150–158, 1983.

[7] R Szeliski, "Rapid octree construction from image sequences," *CVGIP: Image understanding*, vol. 58, no. 1, pp. 23–32, 1993.

[8] JS Franco and E Boyer, "Exact polyhedral visual hulls," in *Conf. BMVC*, 2003, vol. 1, pp. 329–338.

[9] Y Furukawa and J Ponce, "Carved visual hulls for image-based modeling," in *Conf. ECCV*, pp. 564–577. Springer, 2006.

[10] G Vogiatzis, C Hernández, and R Cipolla, "Reconstruction in the round using photometric normals and silhouettes.," in *Conf. CVPR*. IEEE, 2006, vol. 2, pp. 1847–1854.

[11] S Lazebnik, Y Furukawa, and J Ponce, "Projective visual hulls," *IJCV*, vol. 74, no. 2, pp. 137–165, 2007.

[12] M Grum and AG Bors, "3d modeling of multiple-object scenes from sets of images," *Pattern Recognition*, vol. 47, no. 1, pp. 326–343, 2014.

[13] CH Esteban and F Schmitt, "Silhouette and stereo fusion for 3d object modeling," *CVIU*, vol. 96, no. 3, pp. 367–392, 2004.

[14] K Kolev, T Brox, and D Cremers, "Robust variational segmentation of 3d objects from multiple views," in *Pattern Recognition*, pp. 688–697. Springer, 2006.

[15] K Kolev, M Klodt, T Brox, and D Cremers, "Continuous global optimization in multiview 3d reconstruction," *IJCV*, vol. 84, no. 1, pp. 80–96, 2009.

[16] J Heikkila and O Silvén, "A four-step camera calibration procedure with implicit image correction," in *Conf. CVPR*. IEEE, 1997, pp. 1106–1112.

[17] Z Zhang, "A flexible new technique for camera calibration," *TPAMI*, vol. 22, no. 11, pp. 1330–1334, 2000.

[18] C Hernández, F Schmitt, and R Cipolla, "Silhouette coherence for camera calibration under circular motion," *TPAMI*, vol. 29, no. 2, pp. 343–349, 2007.

[19] H Lensch, W Heidrich, and H Seidel, "A silhouette-based algorithm for texture registration and stitching," *Graphical Models*, vol. 63, no. 4, pp. 245–262, 2001.

[20] RV Carvalho, J Kleijn, AH Meijer, and Verbeek FJ, "Modeling innate immune response to early mycobacterium infection," *Computational and mathematical methods in medicine*, vol. 2012, 2012.

[21] JC Lagarias, JA Reeds, MH Wright, and PE Wright, "Convergence properties of the nelder–mead simplex method in low dimensions," *SIAM Journal on optimization*, vol. 9, no. 1, pp. 112–147, 1998.

[22] Y Zhang, BJ Matuszewski, L Shark, and CJ Moore, "Medical image segmentation using new hybrid level-set method," in *5th International Conference on BioMedical Visualization, MEDIVIS'08*. IEEE, 2008, pp. 71–76.